

Experimental and Computational Investigation of Flow Around a 3-1 Prolate Spheroid

D. B. Clarke
Defence Science and Technology Organisation
Maritime Platforms Division
Fishermens Bend, 3207
AUSTRALIA
david.clarke@dsto.defence.gov.au

P. A. Brandner
University of Tasmania
Australian Maritime College
Launceston, 7250
AUSTRALIA
p.brandner@amc.edu.au

G. J. Walker
University of Tasmania
School of Engineering
Hobart, 7001
AUSTRALIA
greg.walker@utas.edu.au

Abstract: The flow around a 3-1 prolate spheroid near the critical Reynolds number is investigated experimentally and numerically. This work was conducted as part of a larger project to examine the flow around Unmanned Underwater Vehicles. The experimental investigation has been performed in a water tunnel at the Australian Maritime College. Fast response pressure probes and a 3-D automated traverse have been developed to investigate the state of the boundary layer. A commercial CFD code has been modified to allow the experimentally determined boundary layer state to be included in the computation. Qualitative and quantitative comparisons between the measured and calculated results are discussed. The tests on the spheroid were conducted within a Reynolds numbers range of 0.6×10^6 to 4×10^6 . The results presented here are for an incidence of 10° .

Key-Words: spheroid, boundary layer, transition, computational, experimental, pressure, flow visualisation

1 Introduction

Unmanned underwater vehicles (UUVs) are used for civilian and military purposes. These applications include surveying coral reefs and seabeds, and mine hunting. When transiting to a region of interest, or surveying a region, they may be required to move quickly. Conversely, detailed investigation of a stationary object requires low speed manoeuvrability. These UUVs operate for at least part of the time at Reynolds numbers where laminar boundary layers may occupy a significant portion of the body surface. Attempting to model the fluid flow around these vehicles using standard implementation of a Reynolds Averaged Navier-Stokes (RANS) turbulence model is likely to result in an inaccurate prediction of body forces and flow structures if the laminar-turbulent transition of the boundary layer is ignored.

In general UUVs are approximately neutrally buoyant, with small control surfaces, so the body of the vehicle provides the dominant component of the hydrodynamic forces. The flow around a 3-1 prolate spheroid was examined in transitional flow conditions, as it provides many of the challenging flow features that occur with a UUV such as:

- three dimensional separation from a curved surface;
- a combination of viscous and form drag where neither dominate;

- regions of laminar and turbulent boundary layer.

Extensive testing has been performed on 6-1 prolate spheroids at Göttingen, Germany. This work has included surface pressure measurements and flow visualisation [15], surface shear stress [16], mean boundary layer profiles, and Reynolds stress [14]. More recently, testing on a 6-1 prolate spheroid has occurred at Virginia Polytechnic Institute and State University [11, 21]. This included the development of a miniature on-board laser doppler velocimeter [7] that allowed measurements in the boundary layer down to $y^+ = 7$.

Several authors have developed numerical techniques for calculating viscous flow, applied them to a spheroid, and compared their predictions to the experimental results previously mentioned. The numerical work has developed from solutions of the boundary layer equations with a predetermined pressure distribution [20]. These were extended to include the prediction of transition [6] from the solution of the Reynolds Averaged Navier-Stokes equations with two-equation turbulence models, Reynolds Stress Models and Detached-Eddy Simulations [8, 13].

This paper provides an overview of the equipment and methodology used to measure the state of the boundary layer on a 3-1 prolate spheroid. It also presents some CFD results with the measured boundary layer state implemented. An incidence of 10° is

selected as it is within the range of incidences a UUV is expected to encounter while transiting, and results in significant non-axisymmetric flow.

2 Experimental Method

The equipment developed to conduct these experiments includes a 3D traversing system, a fast response pressure probe, and the 3-1 prolate spheroid model. In addition, methods were implemented to enable both accurate determination of the model position and examination of boundary layer state. The tests were performed in the Australian Maritime College (AMC) Tom Fink Cavitation Tunnel. This is a closed circuit facility with a test section of $0.6\text{ m} \times 0.6\text{ m} \times 2.6\text{ m}$, a maximum velocity of 12 m s^{-1} , a pressure range of 4 to 400 kPa , and a freestream turbulence intensity of approximately 0.5% [19].

2.1 3-1 Prolate Spheroid Model

The model was designed for measurements of surface pressure, boundary layer state, force and flow visualisation. A single row of tappings running along a meridian from the front to the rear of the model allows the surface pressure to be measured. This row of 21 tappings may be rotated to azimuthal angles, ψ , between -180° and 180° in 15° increments. The angle of incidence, α , of the spheroid may be altered between $\pm 10^\circ$ in 2° increments by switching an internal support. At 0° incidence the major axis of the prolate spheroid model is aligned in the streamwise direction. A grid was marked on the model, at 15 mm and 30° intervals in the x_{bc} and ψ directions respectively, to facilitate flow visualisation. The surface pressure measurements and flow visualisation are used in conjunction with the boundary layer survey to provide a more extensive understanding of the flow than is possible from any one of these techniques in isolation. An exploded image and a photo of the spheroid model are shown in fig. 1 and fig. 2 respectively. The model has a nominal length, L , of 330 mm , with 4 mm truncated from the rear in order to provide access for the sting support. Testing was conducted for Re_L between 0.6×10^6 and 4.0×10^6 , where Re_L is the Reynolds number based on the nominal length of the model. The coordinate system for the model is shown in fig. 3.

2.2 3D Traverse System

The three-dimensional automated traverse has interchangeable probe supports and is capable of operating over the full pressure range of the tunnel. It may be placed in any of the six side window frames of the

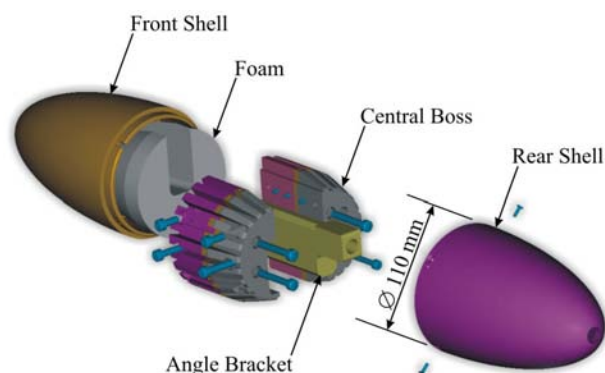


Fig. 1: Exploded View of 3-1 Spheroid Model

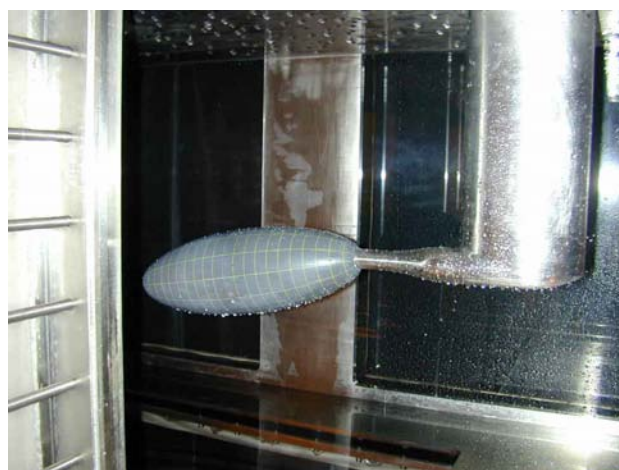


Fig. 2: 3-1 Spheroid Model in Test Section

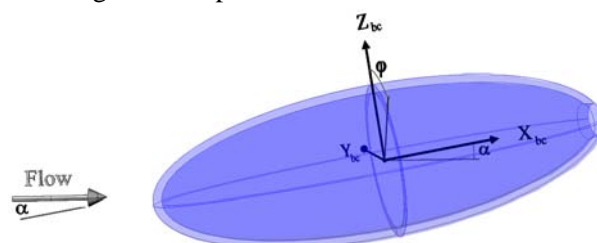


Fig. 3: Coordinate system for 3-1 Spheroid Model

tunnel test section. The main traverse window has a square 225 mm opening that allows access for the probe. The probe is held in position by the traversing plate; it can be positioned $\pm 100\text{ mm}$ vertically from the centre line of the tunnel and $\pm 100\text{ mm}$ horizontally from the centre of the window. The third axis allows the probe to be driven up to 300 mm perpendicular to the side of the tunnel. A hydrofoil-section support is used to minimise probe vibration when the probe is inserted more than 150 mm from the side of the tunnel. A series of thin plates on the inside of the traverse keep the flow around the traversing mechanism streamlined (fig. 4). The traverse is controlled by a closed loop system. The resolution of the traverse in all axes is 0.02 mm , with a positional accuracy of better than 0.1 mm under most conditions.

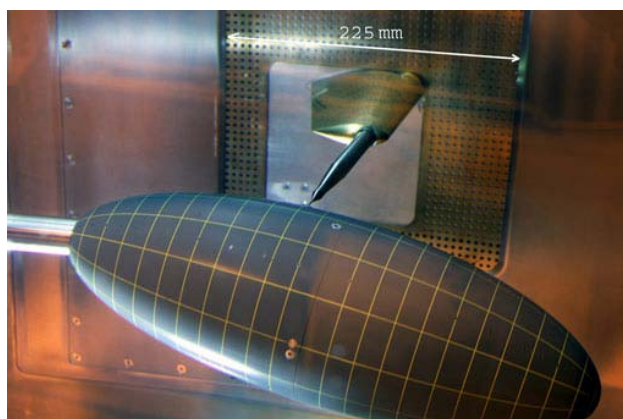


Fig. 4: Traverse Interior

2.3 Fast Response Probe

The fast response probe (FRP) measures the total head with a miniature pressure sensor close to the tip. Placing the sensor close to the tip increases the frequency response of the probe. This probe is similar to those used in transonic [1] and combusting [2] flow applications. The FRP is designed to be modular. It consists of three sections: a probe head, a sensor housing and a support stem. Each section can be changed to suit the flow being measured. The performance of the probe with a 1.2 mm diameter tip and 3.5 bar sensor is detailed in Brandner et al. [3]. For the measurements around the spheroid at an incidence of -10° a 1.0 mm diameter tip was used. For the subsequent tests at 0° and 6° a 0.7 mm diameter tip was developed. The probe was otherwise as detailed in Brandner et al. [3]. The output of the probe has a natural frequency that is a function of the tube dimensions and the stiffness of the probe sensor. The resonance peak due to this natural frequency is filtered, as shown in fig. 5.

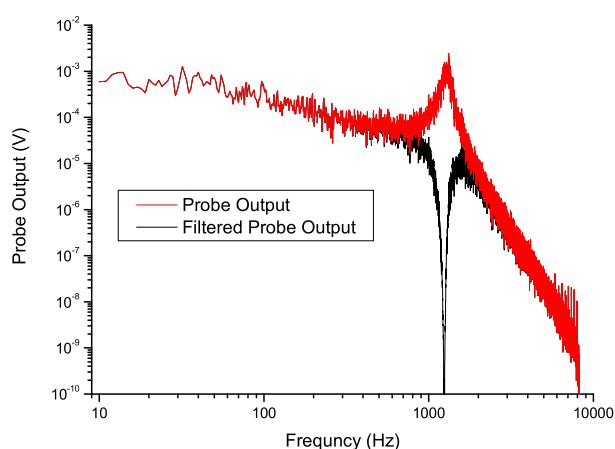


Fig. 5: Frequency Response of FRP with 0.7 mm diameter tip.

2.4 Determining Model Position

The position of the model in traverse coordinates is determined by touching the model at a number of locations with the pitot probe and recording these points. The surface of the model can be described by a quadratic function, so the points at which the probe touch the model (neglecting the offset caused by the finite probe size.) satisfy the following equation:

$$Ax_t^2 + By_t^2 + Cz_t^2 + Dx_t y_t + Ex_t z_t + Fy_t z_t + Gx_t + Hy_t + Iz_t = 1 \quad (1)$$

where x_t , y_t , z_t are the traverse coordinates and A, \dots, I are unknown. As long as nine or more points on the surface of the body are known it is possible to determine the unknowns and thus the offset, orientation and size of the spheroid (or ellipsoid). Although this method was simple to implement, results determined for the unknowns using this solution were sensitive to error in the measurement of the points. This sensitivity is due to equation 1 also being the equation for a number of different surfaces. A failing in this approach is that it does not use all the information that is available, i.e. that the shape is an ellipsoid with axes of known axes lengths a , b and c . The equation of an ellipsoid with its axes aligned to the Cartesian coordinates x_{bc} , y_{bc} , z_{bc} with an offset (x_0, y_0, z_0) is given by

$$\left(\frac{x_{bc} - x_0}{a}\right)^2 + \left(\frac{y_{bc} - y_0}{b}\right)^2 + \left(\frac{z_{bc} - z_0}{c}\right)^2 = 1 \quad (2)$$

Rotating this by $(\phi_t, \theta_t, \psi_t)$ about (z_t, y_t, x_t) respectively provides an equation for the surface of an ellipsoid with known major and minor axes. In order to determine the model's position in traverse coordinates, the orientation $(\phi_t, \theta_t, \psi_t)$ and offset (z_0, y_0, x_0) need to be determined. The non-linear equation obtained from the transformation of equation 2, together with at least six points on the surface of the ellipsoid, may be used to determine the unknowns. The non-linear Levenberg-Marquardt minimisation routine in LabView was modified to handle more than one independent variable to perform the minimisation. In practice about twenty widely spaced points on the surface were measured in order to obtain positioning of the surface to within 0.1 mm. For the spheroidal model there is no requirement to solve for the rotation about the x_{bc} axis.

2.5 Boundary Layer State

The boundary layer is initially laminar at the forward stagnation point. As it moves downstream it may become turbulent. The transition from laminar to turbulent boundary layer flow is described by Emmons [9].

The turbulent boundary layer is characterised by rapid fluctuations in velocity and pressure due to the eddying motion. The start of transition is characterised by short turbulent bursts with rapid velocity and pressure fluctuations. Further downstream the duration and frequency of the turbulent signals increase until the boundary layer is fully turbulent.

Hot films may be placed on the model surface [16], or pressure sensors may be placed flush with the surface or behind pinhole tappings, in order to measure the fluctuations due to turbulence [4]. These two methods have the advantage that they are essentially non-intrusive and allow simultaneous measurements. A disadvantage is that they do not give useful information in regions of separated flow. Each measurement point requires its own transducer and signal conditioning equipment. Hot wire, hot film and pressure probes may be traversed along the surface. These techniques allow for a high density of measurement points. However there are errors associated with the intrusive nature of a probe. Regardless of the sensor, a procedure is required to discriminate between periods of laminar and turbulent flow. Hedley and Keffer [12], together with Canepa [5], provide reviews on a number of these techniques. These methods provide the instantaneous intermittency, γ , which has a value of 1 when the boundary layer is turbulent and 0 when laminar. The time averaged intermittency, $\bar{\gamma}$, is given by

$$\bar{\gamma} = \frac{1}{T} \int_0^T \gamma(t) dt \quad (3)$$

where T is the total sample period and t is time.

The Peak-Valley Counting (PVC) algorithm [18] was used in this work. The detector function was taken as the magnitude of the time derivative of the FRP output squared. The PVC algorithm determines that a peak or valley has been found when the local maxima or minima exceed a threshold S . If another peak or valley occurs within the time window, T_w , the boundary layer is regarded as turbulent for the period between when the threshold was first exceeded and the subsequent peak: accordingly γ is set to 1 for this period. The starting point of the window is brought forward to this next peak and the process is repeated until no peak or valley occurs within the window T_w . On the final peak or valley the turbulent burst is considered to end when the detector function no longer exceeds the threshold. The amplitude of the threshold S and period of time window T_w used with this algorithm were determined experimentally. The threshold amplitude varied between $0.005 kPa^2/\mu s$ at $Re_L = 2.0 \times 10^6$ to $0.070 kPa^2/\mu s^2$ at $Re_L = 4.0 \times 10^6$. A time window of 900 to 700 μs was used for Re_L between 2.0×10^6 and 4.0×10^6 . Examples of the FRP output, detector function and PVC algorithm are

shown in fig. 6 for a measurement on the spheroid.

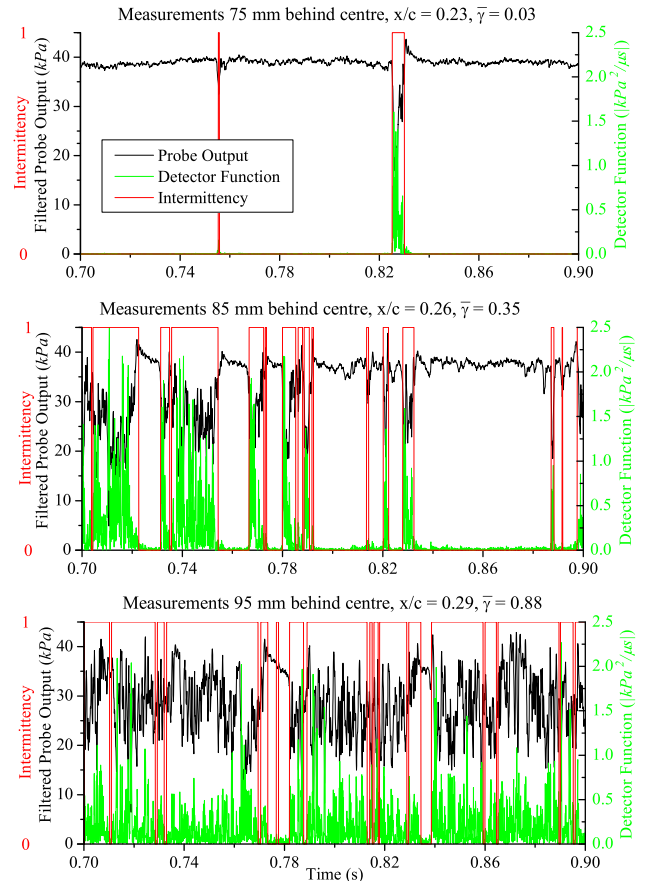


Fig. 6: Intermittency measurements on spheroid with 0.7 mm diameter tip, $Re_L = 3.0 \times 10^6$.

The results for a set of measurements on the spheroid at $Re_L = 4.0 \times 10^6$ are shown in fig. 7. No measurements are reported for $\psi = 0^\circ, -15^\circ, -165^\circ, -180^\circ$ as blockage due to the probe is likely to make these measurements unreliable. For the computational studies the position of the transition at ψ equal -30° will be used for $0^\circ, -15^\circ$; the result at ψ equal -150° will be used for $-165^\circ, -180^\circ$. The transition process was noted to occur over a relatively short proportion of the body length (typically 5%).

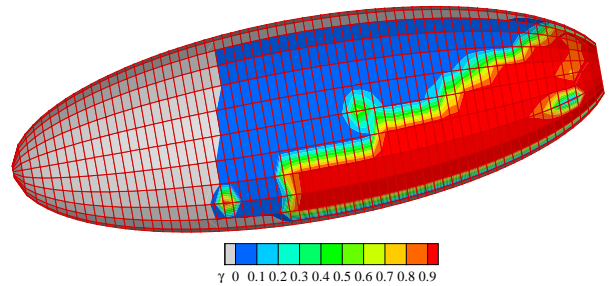


Fig. 7: Measured time averaged intermittency ($\bar{\gamma}$) for spheroid at $Re_L = 4.0 \times 10^6, \alpha = -10^\circ$.

3 Numerical Methods

The commercial CFD code FLUENT 6.2 was used to model these tests. The Fluent preprocessor Gambit was used to create the mesh. The spheroid, sting, foil support and upper limb of the tunnel were modelled using a hybrid mesh with a predominance of hexahedral elements. The volume close to wall faces was meshed with hexahedral elements. The spheroid, sting and foil support were surrounded with an offset volume that allowed fine control of the hexahedral element skewness and grading (fig. 8). This technique allowed elements of high quality to be produced in regions where the fluid was subject to large gradients. The normal distance from the wall of the first element was selected to give $y^+ < 1$ for the spheroid, sting and foil. y^+ values between 30 and 80 were used for the cells adjacent to the tunnel walls. The grading normal to the wall was generally 1.1 or less. Tetrahedral elements were used to link the offset volume and the hexahedral elements used in the majority of the upper limb including the test section. A symmetry plane was used on the vertical x - z plane. Three meshes were used to show grid independence and the negligible impact of the 0.5 mm gap between spheroid and sting with the associated internal volume:

- a standard mesh with 377216 cells in the spheroidal volume adjacent to the spheroid surface (fig. 8);
- a fine mesh was 1101240 cells in the same volume;
- a fine mesh (1101240 cells) with an internal volume between the sting and body.

The results for the forces and moments displayed negligible sensitivity ($\approx 0.5\%$) to an increase in the mesh density or to the inclusion of the small gap and associated internal volume.

The 3D incompressible formulation of the Reynolds-Averaged Navier-Stokes (RANS) equations were solved with the segregated solver. Second-order discretisation was selected for the continuity, momentum and turbulent variables. The SIMPLE algorithm was used for pressure-velocity coupling. Gradient evaluation was performed with a cell-based method.

The enhanced wall function uses a two layer approach with a blending function. If y^+ for the cell nearest the wall is low enough to be inside the viscous sublayer, the flow is modelled to the wall; if y^+ for the cell places it in the log-law region, wall functions are used. A blending function provides a smooth transition for the calculations when the height of the cell adjacent to the wall is such that it is too high to

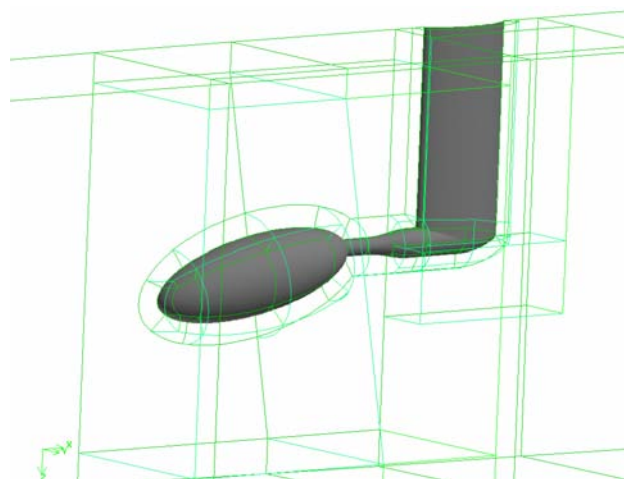


Fig. 8: Geometry for spheroid at $\alpha = -10^\circ$.

fall within the viscous sublayer but too short for the law of the wall to be applicable. The enhanced wall treatment was used for these computations, as it allows for modelling to the wall on the spheroid, sting and support foil. The more economical wall functions were used on the walls of the upper limb.

The realisable $k - \epsilon$ model was selected, as it is reported to be the most suitable of the $k - \epsilon$ turbulence models for handling streamline curvature, separation and vorticity [10]. An added advantage of this model is it has no singularity in the ϵ equation if k is zero. Given the positive performance of the low Reynolds number $k - \omega$ model reported by Kim et al. [13] this was trialled, but produced non-physical results in the total pressure field. This problem has not yet been resolved, and results are not presented for this model. The results of the SST model with a low Reynolds number correction are also compared against experiment, as the developer of the SST model tested it in adverse pressure gradients [17] and reported favourable performance in predicting separation. The inlet boundary conditions were set so the turbulent intensity in the test section was approximately 0.6%.

4 Results and Discussions

4.1 Flow Visualisation at $Re_L = 4.0 \times 10^6$

Surface flow visualisation of the spheroid at $\alpha = -10^\circ$ and $Re_L = 4.0 \times 10^6$ is shown in fig. 9. The surface streamlines calculated for the corresponding conditions using the Realisable $k - \epsilon$ model and the SST model with a Low Reynolds number correction are displayed in figs. 10 and 11 respectively. The calculated surface streamlines for both models predict the large separated region on the side of the model

and the attached flow persisting to almost the base of the model on the suction side of the symmetry plane. The width of this attached flow appears to be more accurately calculated by the realisable model, which is marginally over-predicted. Neither model predicts the flow to stay attached until the base of the model when $\psi < 30^\circ$. On the pressure side the realisable model predicts the flow will stay attached in this region of strong adverse pressure gradient marginally longer than predicted by the SST model. A rapid rise in wall shear stress for both turbulence models is observed near the front of the model. It occurs within the first 5% of the model length on the suction side and within the first 15% on the pressure side. This shows that the calculated turbulent boundary layer is having a significant influence over the majority of the surface model.

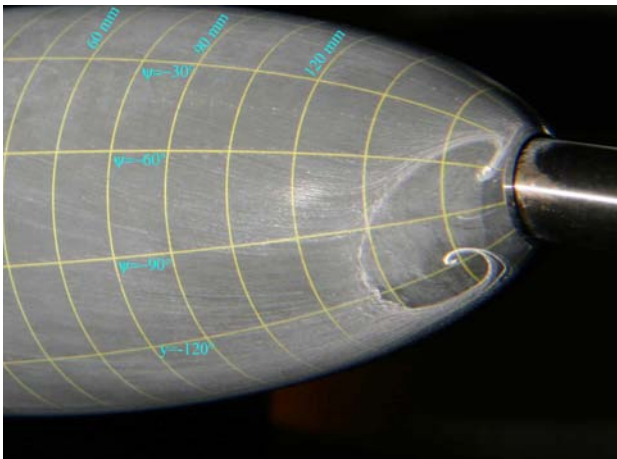


Fig. 9: Flow visualisation on spheroid, $\alpha = -10^\circ$, $Re_L = 4.0 \times 10^6$.

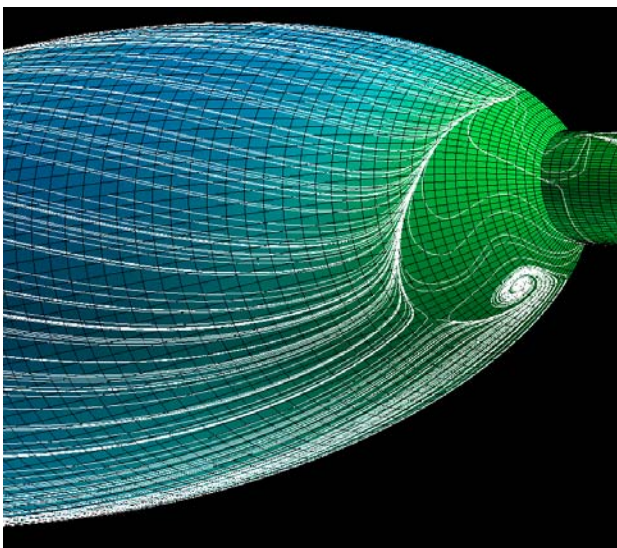


Fig. 10: Surface streamlines calculated using Realisable $k - \epsilon$ model, $\alpha = -10^\circ$, $Re_L = 4.0 \times 10^6$.

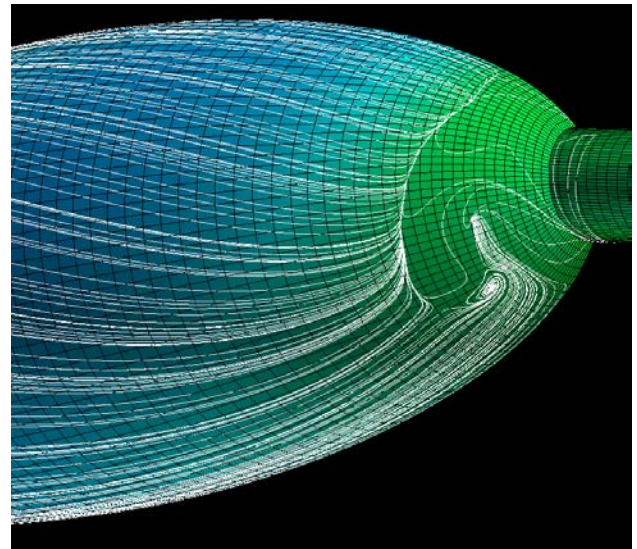


Fig. 11: Surface streamlines calculated using SST Model, $\alpha = -10^\circ$, $Re_L = 4.0 \times 10^6$.

The calculation of the turbulent viscosity was modified via a User Defined Function (UDF) to allow laminar zones to be implemented by switching the turbulent viscosity to zero. For every cell a User Defined Memory (UDM) location was set as an intermittency factor to a value between 0 and 1 indicating a laminar or fully turbulent region respectively. The nominal value for the turbulent viscosity was modified by the intermittency factor. The intermittency factor was determined from the experimental measurements of $\bar{\gamma}$ on the surface of the model. Cells in the boundary layer region normal to the surface were set to a value corresponding to that measured on the surface (fig. 12). This modification provided a small improvement on the pressure side for the realisable model as the predicted flow stays attached until further downstream. A delay in separation is consistent with the thinner boundary layer expected due to the reduced length of turbulent boundary layer. On the suction side the predicted width of attached flow near $\psi = 180^\circ$ appears marginally narrower than shown by the flow visualisation (fig. 13). The results for the SST model with the modification for boundary layer state appeared worse, with a separation bubble being predicted on the pressure side near the base.

4.2 Surface Pressure at $Re_L = 4.0 \times 10^6$

The results of the measured surface pressure for $\psi = -135^\circ$ and -180° over the full range of Re_L are shown in figs. 14 and 15 respectively. In fig. 14 it is apparent that the pressure curves are closely grouped over the front half of the model. Near the centre of the model the curve for the largest Re_L increases a small amount and leaves this grouping. This process

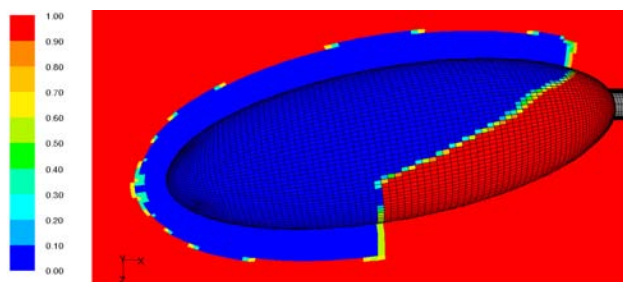


Fig. 12: Intermittency factor for spheroid, $\alpha = -10^\circ$, $Re_L = 4.0 \times 10^6$.

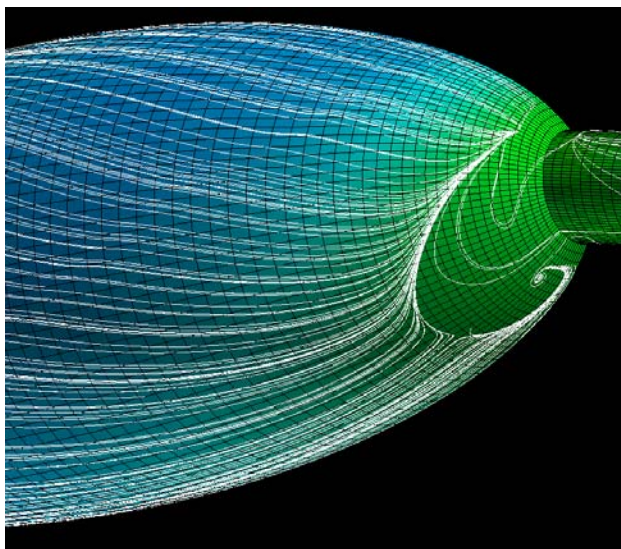


Fig. 13: Surface streamlines calculated using Realizable Turbulence Model with modified boundary layer state, $\alpha = -10^\circ$, $Re_L = 4.0 \times 10^6$.

is repeated a number of times downstream as the surface pressure for the largest Re_L remaining in the initial grouping increases and its associated curve joins the new grouping of curves of larger Re_L . This shift in surface pressure appears to be associated with the process of transition and is most obvious when the pressure gradient is low. The perturbation in the surface pressure field can be explained in terms of the local change in displacement thickness that occurs at the laminar-turbulent transition. This change in displacement thickness creates a discontinuity in the effective surface curvature seen by the free stream, thus creating a perturbation in the pressure that is apparent in the surface pressure measurements. Fig. 15 shows a similar process but the separation of the two curve groups is more pronounced. It also indicates that in this case the transition is upstream of the location used in these calculations at this azimuth. A similar deviation in the surface pressure is apparent near the nose in the results of Meier and Kreplin [15].

Figs. 16 and 17 present a comparison between

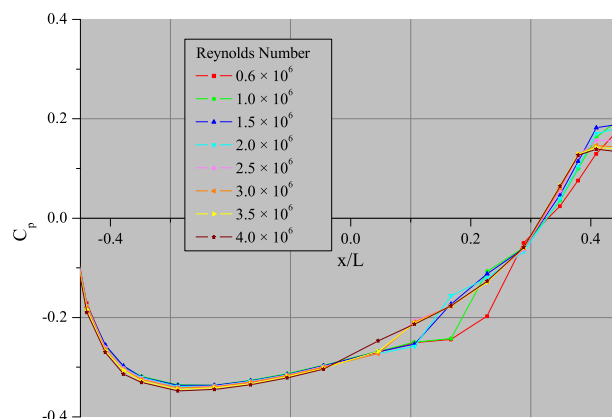


Fig. 14: Surface pressure on spheroid. $\alpha = -10^\circ$, $\psi = -135^\circ$.

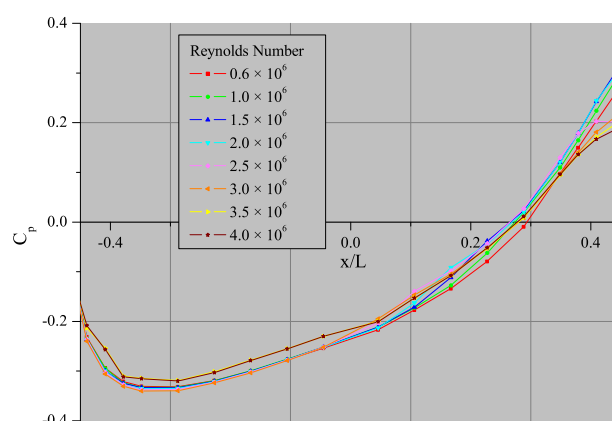


Fig. 15: Surface pressure on spheroid. $\alpha = -10^\circ$, $\psi = -180^\circ$.

the measured and calculated surface pressure. Due to the sensitive nature of transition the position of transition measured using the traverse and the kink in the surface pressure measurements may not always coincide, as these tests were performed during different setups. It should be noted that the most downstream measured data point at each azimuth is the internal base pressure.

The pressure measurements also indicate that transition has occurred near the nose ($x/L = -0.4$) for $\psi = 0^\circ$ at a Re_L of 4.0×10^6 , rather than closer to the base of the body as used for the computations. For this azimuth at $Re_L = 3.5 \times 10^6$, the associated curve is grouped with the lower Reynolds number curves until close to the base, indicating the sensitive nature of the transition for these conditions. Fig. 16 shows the measured result for these two Reynolds numbers at this azimuth. The pressure calculations show little difference regardless of whether the boundary layer is laminar or turbulent over the forward three-quarters of the body; this is contrary to the measured result.

This also means the difference between the implemented transition point and the position implied by the pressure measurements at $\psi = 0^\circ$ should have only a minor influence on the surface pressure calculations. It is suspected that some values of ψ for Re_L of 3.5×10^6 and 4.0×10^6 the disturbance caused by the holes for the pressure taps (0.9 mm diameter) has caused the transition to move upstream. Hence discretion needs to be exercised when using these results.

A deviation in the surface pressure near the location where the turbulence models are switched on is apparent, but it is significantly smaller than that observed in the measured results when transition occurs. Over the majority of the body the implementation of the laminar regions has led to no overall improvement or degradation in the accuracy of the predicted surface pressure. The exception to this is in the separated region on the side of the model where the calculations of the pressure are consistently further from the measured results. The results from the SST model with no laminar region provide the closest match to the measured values in this region.

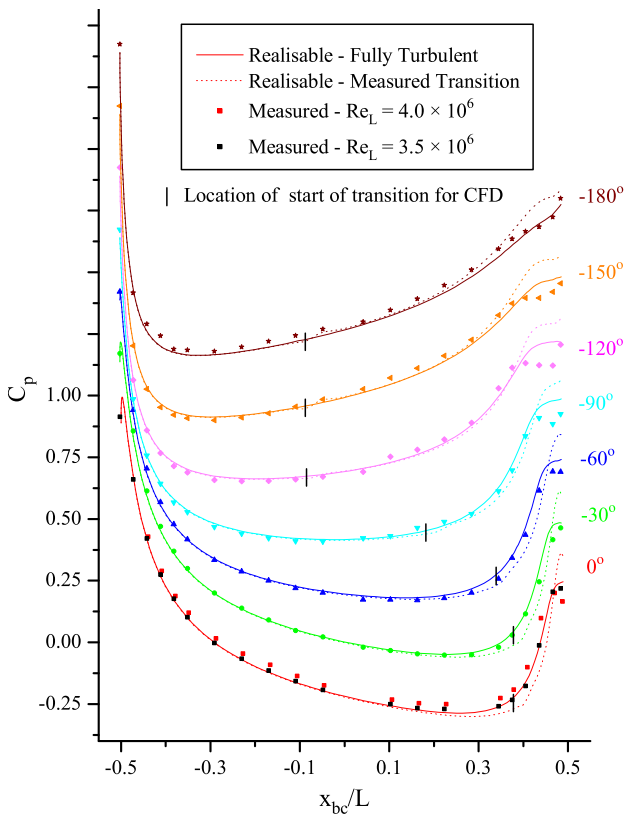


Fig. 16: Comparison of measured and calculated surface pressure using Realisable $k-\epsilon$ turbulence model. $\alpha = -10^\circ$, $Re_L = 4.0 \times 10^6$. (Note :- C_p axis aligned with measurement for 0° ; each subsequent set of curves shifted 0.25 vertically.)

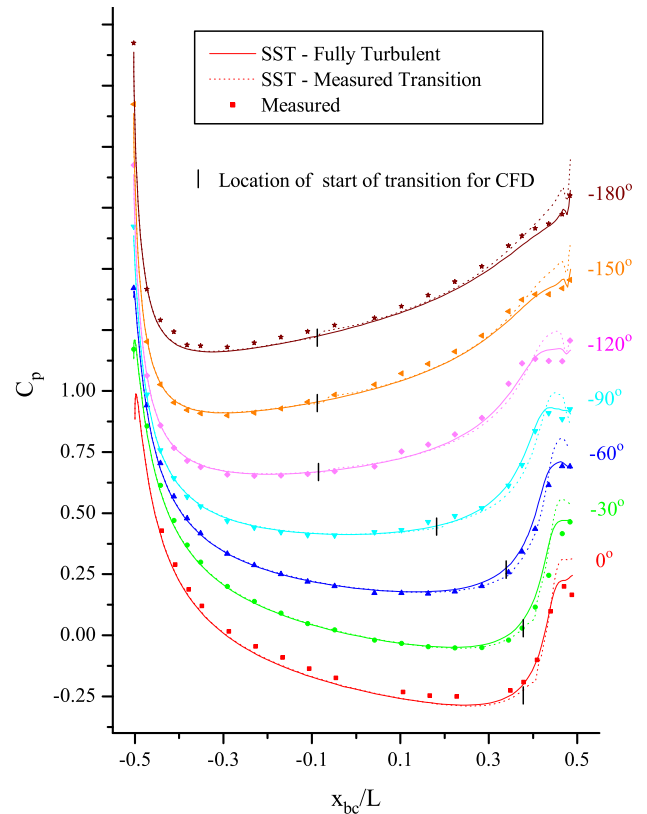


Fig. 17: Comparison of measured and calculated surface pressure using SST turbulence model, $\alpha = -10^\circ$, $Re_L = 4.0 \times 10^6$. (see note with fig. 16).

4.3 Flow Visualisation at $Re_L = 2.0 \times 10^6$

Assessment of the turbulence models tested at $Re_L = 4.0 \times 10^6$ with and without the inclusion of the laminar zones was expanded to examine the case at $Re_L = 2.0 \times 10^6$. Contamination of the spheroid surface for this Reynolds number resulted in the boundary layer survey being discarded. Fortunately for this Reynolds number the flow visualisation provides an indication of the boundary layer transition between $\psi = 0^\circ$ and -90° . The location of boundary layer transition was estimated from the increased scouring of the oil apparent in fig. 18. The increased scouring in this case is associated with the greater wall shear present in a turbulent boundary layer. Other photos at this Reynolds number using a less viscous oil suggest that for ψ between 0° and approximately -45° a very short laminar separation bubble exists at the transition region. This laminar separation bubble is not picked up by the surface pressure measurements due to the relatively coarse placement of tappings. Excellent agreement between the flow visualisation and surface pressure measurements for the location of boundary layer transition is shown in fig. 18. This provides confidence in the application of the transition location obtained from the surface pressure measurements to the com-

putational work for this case.

It should be noted that, in the over fifty flow visualisation performed on these models, in only a few cases has the boundary layer transition region been observed with confidence. The high density of water helps obtain high quality surface pressure measurements. Even with high quality surface pressure measurements over a range of Reynolds numbers, boundary layer transition is difficult to determine if the surface pressure is varying rapidly due to other factors (e.g. surface curvature, as noted previously). Neither of these methods determine the length of the transition region, which for the purpose of this computation was taken as 10 mm . This is consistent with the short transition length seen at $\alpha = 6^\circ$ for this Reynolds number.

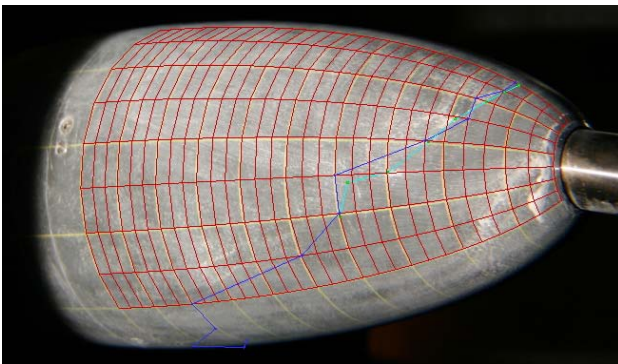


Fig. 18: Flow visualisation on spheroid, $\alpha = -10^\circ$, $Re_L = 2.0 \times 10^6$. Cyan and blue line show estimate of boundary layer transition position from this photo and pressure measurements respectively.

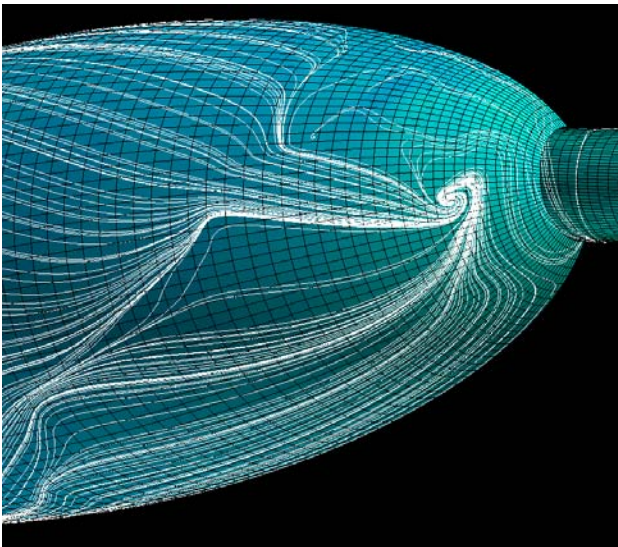


Fig. 19: Surface streamlines calculated using Realisable $k - \epsilon$ turbulence model with modified boundary layer state, $\alpha = -10^\circ$, $Re_L = 2.0 \times 10^6$.

Surface flow visualisation for the computed result at $Re_L = 2.0 \times 10^6$ using the Realisable $k - \epsilon$ turbulence model was similar to that using the same model at $Re_L = 4.0 \times 10^6$. When the region of laminar flow was implemented for this case, the resulting surface flow visualisation (fig. 19) showed a laminar separation for ψ between 0° and -45° ; the velocity vector plot at the cell centres adjacent to the surface confirms that no reattachment occurred behind this separation line. This laminar separation occurs approximately 25 mm upstream of the implemented transition region. The technique of prescribing the transition region is likely to have difficulty modelling laminar separation bubbles as the turbulent region is unable to shift to just downstream of the laminar separation and then adjust with the iterative solution of the flow field.

The major computed vortical structure on the side of the model rotates in the opposite direction to the structure in the photo, it is also positioned further upstream. The photograph show no funnelling of the flow into the vortical structure from fluid at the side ($\psi = -75^\circ$ to 120°) of the model as depicted in fig. 19.

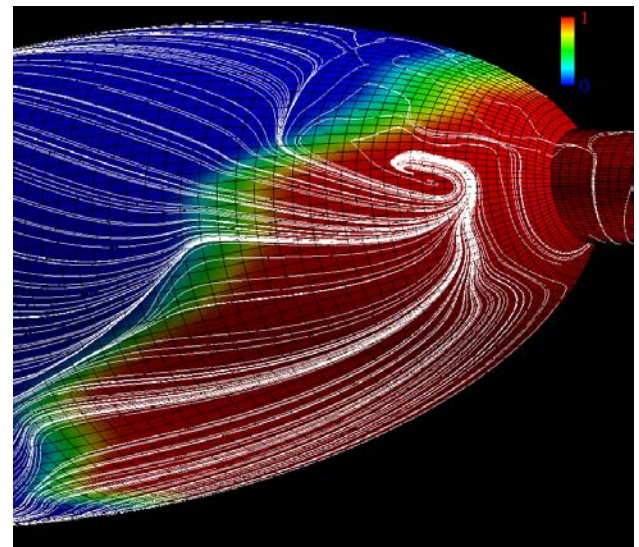


Fig. 20: Surface streamlines calculated using Realisable $k - \epsilon$ turbulence model with lengthened transition region, $\alpha = -10^\circ$, $Re_L = 2.0 \times 10^6$. Surface contours showing time averaged intermittency ($\bar{\gamma}$).

The implementation of the transition region in a steady state solver is by necessity only spatial, while the actual process has an additional temporal component. Concern that the implementation of the transition region may be encouraging flow separation or redirecting the surface flow by providing a sudden discontinuity in the surface shear stress was tested

by increasing the length of the transition region to 25 mm, thus reducing the sharpness of the discontinuity. Fig. 20 shows the redirection of the flow has been reduced by the increased length of the transition region but is still clearly apparent. No redirection of the flow is apparent in the boundary layer transition region in fig. 18. The results with the SST model with the low Reynolds Number correction were of no greater accuracy and are not further reported.

4.4 Drag

Although no drag measurements are available for comparison it is worth noting the computed breakdown between form and viscous drag. The calculated C_d based on the maximum cross-section perpendicular to the x_{bc} is given in table 1. The values in this table demonstrate the necessity of implementing the correct boundary layer regime if the drag is to be accurately calculated on a body where no one boundary layer type dominates. An artificially long region of turbulent flow will increase the viscous drag, due to the greater shear stress associated with the turbulent flow, and increase the form drag as its faster boundary layer growth results in a thicker boundary layer that will separate earlier.

Turbulence Model	Form	Viscous	Total
Realisable	0.0128	0.0183	0.0311
SST Low Re	0.0144	0.0173	0.0317
Realisable + Lam	0.0076	0.0079	0.0155
SST Low Re + Lam	0.0113	0.0074	0.0187

Table 1: Calculated Drag Coefficients for $\alpha = -10^\circ$, $Re_L = 4.0 \times 10^6$.

5 Conclusions

The turbulence models used in the analysis at $Re_L = 4.0 \times 10^6$ with and without the modification for laminar regions do a reasonable job of calculating the surface pressure and surface streamlines. Although this implementation of laminar regions of flow in the CFD has not led to an improvement in calculation of the surface pressure, the ability to allow for laminar regions of flow is critical in the calculation of drag on bodies with a significant portion of laminar flow. The minimal variation in surface pressure predicted between the laminar and turbulent flow is in contrast to the measured results. The cause of this discrepancy warrants further investigation. Prescribing the transition region in the region of a laminar separation bubbles was unsuccessful at $Re_L = 2.0 \times 10^6$.

Acknowledgements: The authors wish to acknowledge the contribution of: Mr John Xiberras in the detailed design of the spheroid and support foil; Mr Vinh Nguyen in the detailed design of the 3D Traverse; Mr Paul Cooper and Mr Paul Vella in the manufacture of the spheroid, support foil and traverse; Mr Sasha Smiljanic in the design of the electronics and software for the traverse controller; and Mr Robert Wrigley for onsite manufacture and fitting. The support of DSTO and AMC has also been vital.

References:

- [1] Biagioni, L. and d'Agostino, L., *Measurement of Energy Spectra in Weakly Compressible Turbulence*, AIAA 99-3516, 30th AIAA Fluid Dynamics Conference, 1999.
- [2] Bradshaw, P., *An Introduction to Turbulence and its Measurement*, Pergamon Press, 1971.
- [3] Brandner, P.A., Clarke, D.B. and Walker, G.J., *Development of a Fast Response Pressure Probe for Use in a Cavitation Tunnel*, 15th Australasian Fluid Mechanics Conference, 2004, 4 pp. (On C.D.)
- [4] Bull M.K., *Wall-Pressure Fluctuations Beneath Turbulent Boundary Layers: Some Reflections on Forty Years of Research*, Journal of Sound and Vibration, 190(3), 1996, 299-315.
- [5] Canepa E., *Experiences in the Application of Intermittency Detection Techniques to Hot-Film Signals in Transitional Boundary Layers*, The 16th Symposium on Measuring Techniques in Transonic and Supersonic Flow in Cascades and Turbomachines, September 23-24, 2002, Cambridge, United Kingdom, 10 pp.
- [6] Cebeci T., Chen H.H. and Arnal D. and Huang T.T., *Three-Dimensional Linear Stability Approach to Transition on Wings and Bodies of Revolution at Incidence*, AIAA Journal, Vol. 29, No. 12, 1991, 2077-2085.
- [7] Chesnakas C.J. and Simpson R.L., *Full three-dimensional measurements of the cross-flow separation region of a 6:1 Prolate Spheroid*, Experiments in Fluids, Vol. 17, No 1, 1994, 68-74.
- [8] Constantinescu G.S., Pasinato H., Wang Y, Forsythe J.R. and Squires K.D. *Numerical Investigation of Flow Past a Prolate Spheroid*, ASME J. Fluids Eng., Vol. 124, 2002, 904-910.
- [9] Emmons H. W., *The Laminar-Turbulent Transition in a Boundary Layer Part 1*, Journal of the Aeronautical Sciences, Vol. 18, No 7, 1951, 490-498.

- [10] *Fluent 6.2 Users Guide* Fluent Inc., 2005.
- [11] Goody M., Simpson R.L., Engel M., Chesnalas C. and Devenport W., *Mean Velocity and Pressure and Velocity Spectral Measurements within a Separated Flow Around a Prolate Spheroid at Incidence*, AIAA Paper 98-0630, 1998, 10 pp.
- [12] Hedley T.B. and Keffer J.F., *Turbulent/Non-Turbulent Decisions in an Intermittent Flow.*, J. Fluid Mech. Vol. 64, part 4, 1974, 625–644.
- [13] Kim S.E., Rhee S.H. and Cokljat Davor, *Application of Modern Turbulence Models to Vortical Flow Around a 6:1 Prolate Spheroid at Incidence.*, AIAA 2003-429, 2003, 11 pp.
- [14] Kreplin, H.P. and Stäger, R., *Measurements of the Reynolds-Stress Tensor in the Three-Dimensional Boundary Layer of an Inclined Body of Revolution.*, Ninth Symposium on "Turbulent Shear Flows", Dept. of Mechanical Engineering, Kyoto Univ, Japan, August, 1993, pp. 2-4-1 – 2-4-6.
- [15] Meier, H.U. and Kreplin, H.P., *Pressure Distributions and Flow Visualisations on an Ellipsoid 1:6 Designed for Three-Dimensional Boundary Layer Investigations.*, Proc. 7th US/FRG DEA-Meeting, AFFDL-TR-78-111, 1978, 197–208.
- [16] Meier, H.U. and Kreplin, H.P., *Experimental Investigation of the Boundary Layer Transition and Separation on a Body of Revolution*, Zeitschrift f. Flugwiss. Weltraumforsch., Vol. 4, 1980, 65–71.
- [17] Menter, F.R., *Two-Equation Eddy-Viscosity Turbulence Models for Engineering Applications*, AIAA Journal, Vol.32, No. 8, 1994, 1598–1604.
- [18] Solomon, W.J., *Unsteady Boundary Layer Transition on Axial Compressor Blades*, Ph.D. thesis, University of Tasmania, 1996.
- [19] Brandner, P.A. and Walker G.J., *An Experimental Investigation into the Performance of a Flush Water-jet Inlet*, Journal of Ship Research, SNAME, Vol 51, No. 1, March 2007.
- [20] Wang K.C., *Boundary layer over a blunt body at low incidence with circumferential flow.*, J. Fluid Mech, Vol. 72, 1975, 39–65.
- [21] Wetzel, T.G., Simpson R.L. and Cheesnakas, C.J., *Measurement of Three-Dimensional Cross-flow Separation.*, AIAA Journal, Vol. 36, No 4, 1998, 557–564.